



# Viscous-flow Calculations of Submarine Maneuvering Hydrodynamic Coefficients and Flow Field based on Same Grid Topology

L. Cao<sup>1†</sup>, J. Zhu<sup>1</sup> and G. Zeng<sup>2</sup>

<sup>1</sup> Department of Naval Architecture and Ocean Engineering, Naval University of Engineering, Wuhan 430033, China

<sup>2</sup> Navy Submarine Academy, Qingdao 266042, China

†Corresponding Author Email: caoliushuai@hrbeu.edu.cn

(Received January 20, 2015; accepted April 15, 2015)

## ABSTRACT

To estimate the maneuverability of a submarine at the early design stage, an accurate evaluation of the hydrodynamic coefficients is important. In a collaborative exercise, the authors performed calculations on the bare hull DRAPA SUBOFF submarine to investigate the capability of viscous-flow solvers to predict the forces and moments as well as flow field around the body. A typical simulation program was performed for both the steady drift tests and rotating arm tests. The same grid topology based on multi-block mesh strategy was used to discretize the computational domain. A procedure designated drift sweep was implemented to automatically increment the drift angle during the simulation of steady drift tests. The rotating coordinate system was adopted to perform the simulation of rotating arm tests. The Coriolis force and centrifugal force due to the computation in a rotating frame of reference were treated explicitly and added to momentum equations as source terms. Lastly, the computed forces and moment as a function of angles of drift in both conditions are compared with experimental results and literature values. They always show the correct trend. Flow field quantities including pressure coefficients and vorticity and axial velocity contours are also visualized to vividly describe the evolution of flow motions along the hull.

**Keywords:** Viscous-flow; Maneuvering; Hydrodynamic coefficients; Flow field.

## 1. INTRODUCTION

The missions being proposed for submarines by both military and naval architects are becoming increasingly complex and challenging. In order to meet these demands the next generation of submarines will need to be faster, to operate for longer durations, and to be more maneuverable than existing vehicles. A useful tool for gaining an understanding of the performance of a submarine is a dynamic simulation of the equations of motion of the vehicle. To perform these simulations the hydrodynamic coefficients of the vehicle must first be provided. These coefficients are always determined by model tests, analytical semi-empirical methods and a combination of both. With the development of computational resources, computational fluid dynamics (CFD) can also play an important role here by providing an easier and more accurate determination of these loads.

At the very beginning, hydrodynamic model tests have been done in a number of different facilities for a wide range of different configurations to

achieve the hydrodynamic data. Feldman (1995) conducted straight-line and rotating arm captive-model experiments to investigate stability and control characteristics of submarines and submersible vehicles. Lloyd and Campbell (1986) and Lloyd (1988) performed a thorough experimental program to investigate the vorticity shed by a body of revolution in curved flow. Model tests for submarines are time consuming and expensive, which involve model building, testing, analyzing, and interpreting the results. Costs can be even higher when the vehicle configuration may be changed many times.

Analytical and semi-empirical (ASE) methods have been used for years to predict the maneuvering performance of marine vehicles. ASE methods are directly focused on the estimation of parameters such as added mass and inertias coefficients, linear and nonlinear damping coefficients, and control action related parameters. The report by Peterson (1980) is one of the most comprehensive. This provides a description and comparison of seven widely used semi-empirical methods for predicting

several important linear hydrodynamic coefficients for conventional marine vehicles. The seven methods are compared by applying them to three torpedoes and three submersibles for which experimental data are available. Nahon (1993) described how to determine underwater vehicle hydrodynamic derivatives using the USAF Datcom method. Holmes (1995) illustrated the application of the Datcom method to predict the hydrodynamics coefficients utilizing geometric considerations. The hull shape considered was a body of revolution having a basic submarine shape. De Barros *et al.* reviewed (2006) the use of ASE methods to predict the hydrodynamic derivatives of AUVs and compared (2008) the results with that of CFD methods. Although ASE methods can give a rapid estimate of the hydrodynamic coefficients, but they are not accurate enough because they always disregard non-linear and viscous effects.

Recently, with the rapid development of computational resources, applying CFD methods to construct the flow field and calculate the hydrodynamic loads acting upon marine vehicles has been sprung out. Plenty of authors have published their papers in dealing with the determination of forces and moments (Vaz *et al.*, 2010), the influence by using different turbulence closure models (Phillips *et al.*, 2010; Sakthivel *et al.*, 2011), the verification and validation of the results (Simonsen *et al.*, 2003; Zhang, 2010), the comparison of dynamic characteristics of different geometries and configurations (Wang *et al.*, 2014), and even the real simulation coupled with motions via overlapping grid techniques (Carrica *et al.*, 2012) as well as the optimization process (Rajabi and Kavianpour, 2014). As recently reviewed by Stern *et al.* (2013) and Stern *et al.* (2014), CFD capabilities continue to advance at even faster speed, and are changing the face of shipbuilding industry by transforming the build-and-test design spiral approach to the simulation-based design (SBD) approach.

As a former work stepping into the SBD and optimization process, the main objective of this paper is to perform two kinds of virtual captive-model experiments on a submarine to obtain the hydrodynamic coefficients. The organization of this paper is as follows. Section 2 gives the geometric information of DRAPA SUBOFF model. The numerical methods adopted to undertake the computation are addressed in Section 3 in detail. In Section 4, the calculation results are compared with the experimental results and literature values, and the flow field quantities are visualized. Lastly, the conclusions are drawn in Section 5.

## 2. TEST CASE AND SIMULATION CONDITIONS

The submarine model used in this study was the SUBOFF model. The bare hull configuration considered consists of an axisymmetric body without sail or any other appendages. The main particulars of the SUBOFF hull form are given in Table 1 (Groves *et al.*, 1989).

**Table 1 Principal particulars of DRAPA SUBOFF submarine**

| Description            | Symbol    | Magnitude       | Unit  |
|------------------------|-----------|-----------------|-------|
| Overall length         | $L_{oa}$  | 4.356           | m     |
| Perpendicular length   | $L_{pp}$  | 4.261           | m     |
| Maximum hull diameter  | $D_{max}$ | 0.508           | m     |
| Center of buoyancy     | $x_B$     | 0.4621 $L_{oa}$ | m     |
| Volume of displacement | $\nabla$  | 0.708           | $m^3$ |
| Wetted surface         | $S_{wa}$  | 5.998           | $m^2$ |

The calculation cases have been chosen to coincide with the results of captive-model tests available. The steady drift tests and rotating arm tests were performed in the David Taylor Model Basin in Naval Surface Warfare Center, Carderock Division (NSWCCD), reported by Roddy (1990) and Toxopeus (2012), respectively. During the rotating arm tests, the model was forced in a turn to starboard. The non-dimensional angular velocity  $\gamma$  is defined as:

$$\gamma = \frac{r \cdot L_{oa}}{V_0} = \frac{L_{oa}}{R} \quad (1)$$

with  $V_0$  the velocity of the center of buoyancy and  $R$  the turning radius. The detailed simulation conditions for both steady drift tests and rotating arm tests are described in Table 2.

**Table 2 Simulation conditions for steady drift tests and rotating arm tests**

| Item                    | Steady drift tests                   | Rotating arm tests            |
|-------------------------|--------------------------------------|-------------------------------|
| Reynolds number         | $12 \times 10^6$                     | $6.53 \times 10^6$            |
| Velocity [m/s]          | 2.7631                               | 1.5036                        |
| Drift angle $\beta$ [°] | 0, 1, 2, 4, 6, 8, 10, 12, 14, 16, 18 | 0, 2, 4, 6, 8, 10, 12, 14, 16 |
| $\gamma$                | 0                                    | 0.1, 0.2, 0.3, 0.37, 0.5      |

## 3. NUMERICAL METHODS

### 3.1 Mathematical Methods and Turbulence Model

Three dimensional Reynolds Averaged Navier-Stokes (RANS) equation for incompressible flow along with continuity equation are given below:

$$\frac{\partial \overline{U}_i}{\partial x_i} = 0 \quad (2)$$

$$\rho \frac{\partial \overline{U}_i}{\partial t} + \rho \frac{\partial \overline{U}_i \overline{U}_j}{\partial x_j} = - \frac{\partial P}{\partial x_i} + \frac{\partial}{\partial x_j} \left\{ \mu \left( \frac{\partial \overline{U}_i}{\partial x_j} + \frac{\partial \overline{U}_j}{\partial x_i} \right) \right\} - \rho \frac{\partial \overline{u'_i u'_j}}{\partial x_j} + f_i \quad (3)$$

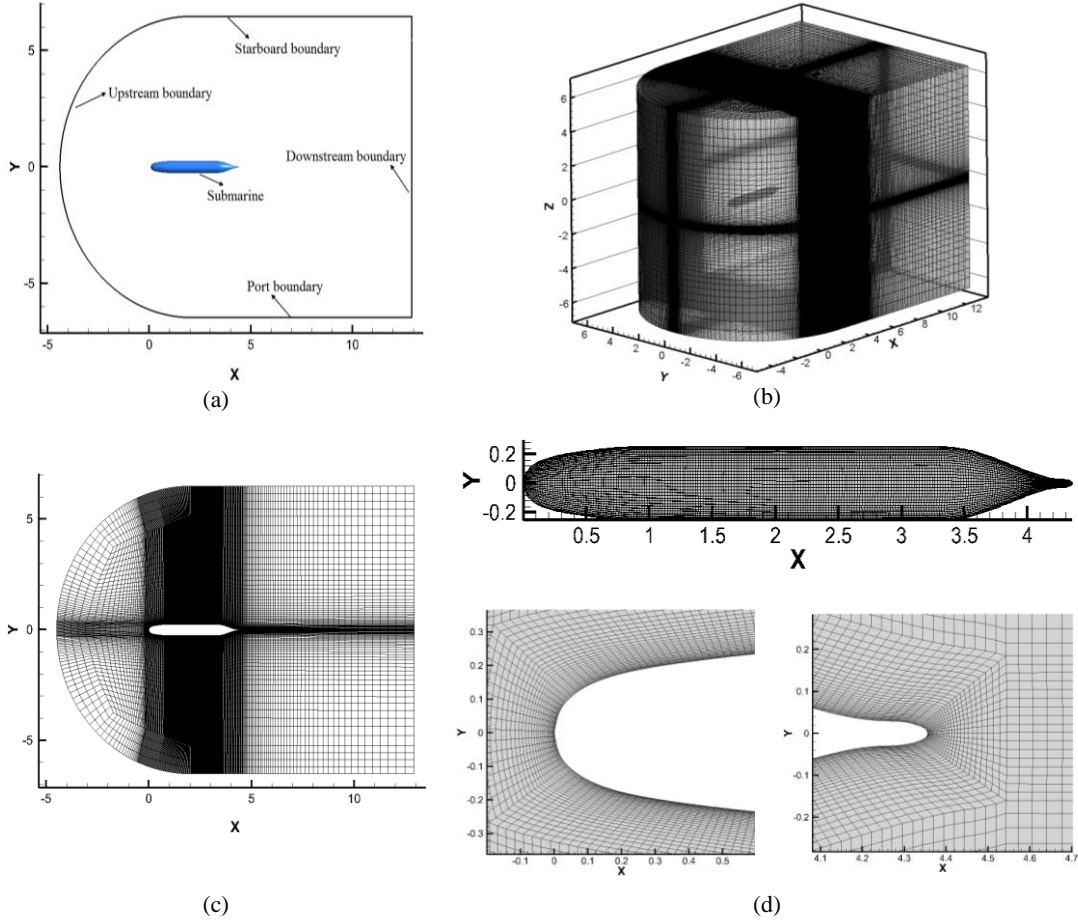


**Fig. 1. (a) Computational domain, (b) mesh total domain, (c) mesh cut plane  $z=0$ ,  
(d) hull surface mesh and mesh cut plane for the bow and stern.**

where  $\bar{U}_i$  is the mean Cartesian flow field and  $P$  is the mean pressure of the water around the hull,  $f_i$  represents the external forces,  $\rho\bar{u}_i'\bar{u}_j'$  is the Reynolds stress tensor.

Assuming a steady flow, the rotational motion can be simulated by implementing the Coriolis force and centrifugal force due to the rotation of the coordinate system as additional source terms, such that the modified external forces reads:

$$f_i = -\rho \left( 2\bar{\Omega} \times \bar{u} \right)_i - \rho \left( \bar{\Omega} \times (\bar{\Omega} \times \bar{r}) \right)_i \quad (4)$$

with  $\bar{\Omega}$  the vector of rotation,  $\bar{u} = (u_1, u_2, u_3) = (u, v, w)$  the velocity vector and  $\bar{r} = \bar{x} - \bar{x}_R$  the radius of rotation, where  $\bar{x}_R$  indicates the position of the center of rotation. In the equation above, the Coriolis force is represented by  $-\rho(2\bar{\Omega} \times \bar{u})$  while the centrifugal force is  $-\rho(\bar{\Omega} \times (\bar{\Omega} \times \bar{r}))$ . Note that, even though these two forces are moderate for a submarine model in steady turn, the results are completely wrong if they are neglected (Hochbaum, 1998).

To close the equation set, the RNG  $k - \varepsilon$  turbulent model with wall functions was adopted. The RNG  $k - \varepsilon$  model was derived using a statistical technique called renormalization group theory. It is similar in form to the standard  $k - \varepsilon$  model, but includes some refinements to make it more accurate and reliable for a wider class of flows, especially for swirling flows.

### 3.2 Computational Domain and Grids

The computational domain is illustrated in Fig.1. (a). It extends  $1.5L_{oa}$  upstream and  $2L_{oa}$  downstream and  $1.5L_{oa}$  transversely. Blocked-based structured grids were built using the commercial software ICEM CFD. A twofold O-grid topology was applied around the hull; the inner zone, extending to about twice the trailing edge boundary thickness, was designed to capture the boundary layer and flow separation; the outer zone was used to provide a fine mesh density to resolve the flow field and offer a balance of resolution and processing time.

As described above, the RNG  $k - \varepsilon$  turbulence model with wall functions was adopted in this paper. The wall treatment associated with the turbulence model requires  $y^+$  at the centroid of the

**Table 3 Values of non-dimensional drag for different grid density**

| Grid   | Refinement Ratio                    | No. of Cells | Grid Size (streamwise direction×lateral direction×vertical direction) | Non-dimensional Drag |
|--------|-------------------------------------|--------------|---|----------------------|
| Grid 1 | Base grid                           | 456300       | 169×54×50   | 1.165e-03            |
| Grid 2 | Grid 1 ×( $\sqrt{2}$ ) <sup>3</sup> | 1307808      | 239×76×72   | 1.082e-03            |
| Grid 3 | Grid 2 ×( $\sqrt{2}$ ) <sup>3</sup> | 3723408      | 338×108×102   | 1.020e-3             |
| Grid 4 | Mean of Grid 2&3                    | 2339744      | 289×92×88   | 1.041e-3             |

layer closest to the wall be within 30 to 300, where  $y^+$  is a non-dimensional distance perpendicular to the wall. Initially, the first cell thickness can be estimated using the following empirical equation (ANSYS, 2012):

$$y = L_{oa} y^+ \sqrt{80} Re^{-13/14} \quad (5)$$

For a target  $y^+ \approx 50$ , the mesh was generated for the computational domain with 31 elements in the boundary layer.

For the grid independence analysis, four different grids (Grid 1, Grid 2, Grid 3 and Grid 4) based on the first set grid were generated. Initially, Grid 1 was chosen as base grid which is relatively coarser. The grid refinement ratio was determined according to the ITTC manual (1999). The grid refinement ratio  $\sqrt{2}$  was applied in each direction to get a finer grid from Grid 1. The details of the grids used for the study were shown in Table 3. The non-dimensional drag was observed to be almost same for Grid 2, Grid 3 and Grid 4 in straight ahead simulation. Hence for all further calculations, Grid 4 is chosen for a balance of computational cost and accuracy. The schematic of the computational domain, the grid of the whole domain, the mesh cut plane  $z=0$ , the hull form and the bow and stern part of the hull are revealed in Fig. 1 (a)-(d), respectively.

### 3.3 Boundary Conditions and Solver Setup

There are four boundary conditions utilized in the paper. In Fig.1 (a) the upstream and the port and starboard boundaries are treated as velocity inlet boundaries on which velocity components are imposed. In steady drift cases, the velocity components vary with the angle of drift. As for the rotational cases, the velocity magnitude is proportional to the distance away from the rotational center and the absolute value of angular velocity, and is perpendicular with the positional vector directed towards the rotational center. The downstream boundary is specified to be a pressure outlet and the top and bottom boundaries are free slip walls. No slip condition is specified for the hull body.

All calculations were performed with the commercial viscous-flow solver ANSYS FLUENT, which utilizes the finite volume method to solve the governing integral equations for the conservation of

mass and momentum. The used discretization schemes were the standard for the pressure, the SIMPLE for the pressure-velocity coupling. The turbulence energy and the specific dissipation were discretized with second-order upwind schemes. The source terms and the velocity components defined in rotational cases mentioned above are incorporated in ANSYS FLUENT solver through User Defined Functions (UDF). So the same grid topology is used for both steady drifts cases and rotational cases, this is helpful in dealing with optimization problem where dozens of configurations have to be handled.

## 4. RESULTS AND DISCUSSION

### 4.1 Forces and Moments

A procedure was implemented to automatically increment the drift angle during a single simulation in order to efficiently generate results for many drift angles. Simulations begin at an initial drift angle 0°, when a specified number of iterations is reached, the drift angle is incremented by  $\Delta\beta$  (by changing the inflow conditions) and the solution is continued from the solution at the previous drift angle. Starting the calculations from a converged solution at a slightly different drift angle saves time and improves accuracy. This procedure is repeated until the desired maximum inflow angle is reached. This procedure was designated drift sweep and the application has already been presented in Toxopeus (2011) and Cao and Zhu (2014), respectively. The computational longitudinal force, lateral force, and yaw moment curves versus iterations are shown in Fig.2 (a)-(c). Fig.2 (d)-(f) reveals the non-dimensional drag and lateral forces and yaw moment

( $X, Y = F_x, F_y / \frac{1}{2} \rho V_0^2 L_{pp}^2$ ,  $N = M_z / \frac{1}{2} \rho V_0^2 L_{pp}^3$ ) as a function of the drift angle, respectively.

The predicted forces and moment on the hull during the turn as a function of the drift angle are presented in Fig.3. When the angle of drift is increased, the variation of force became nonlinear. There is a significant increase in the slope of force coefficient. Figs. 2-3 show very good agreement between CFD and experimental results, as well as literature values, thus adding credibility to the analysis based on the CFD flow visualization that follows. Table 4 shows the static and rotary maneuvering coefficients estimated from the calculated data.

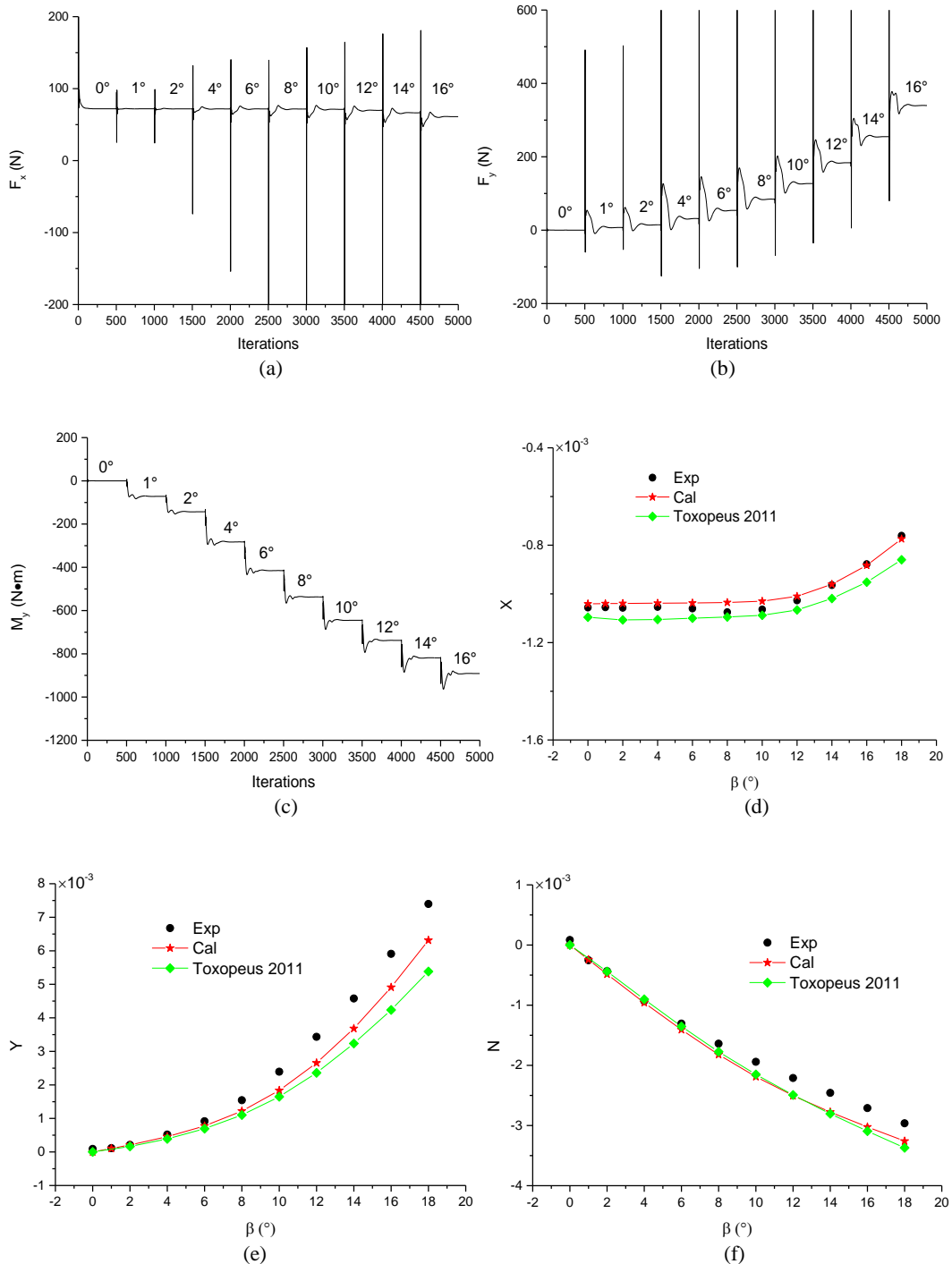


**Fig. 2.** (a)-(c) The longitudinal force, lateral force and yaw moment curves versus iterations during drift sweep procedure; (d)-(f) non-dimensional drag, lateral force and yaw moment as a function of the drift angle in steady drift tests simulation.

**Table 4** Maneuvering coefficients estimated from experiments compared with that of CFD and ASE

| Item   | Exp                      | Cal                      | Error (%) | ASE                      | Error (%) |
|--------|--------------------------|--------------------------|-----------|--------------------------|-----------|
| $Y'_v$ | $-5.948 \times 10^{-3}$  | $-5.804 \times 10^{-3}$  | 2.42      | $-7.013 \times 10^{-3}$  | -17.91    |
| $N'_v$ | $-12.795 \times 10^{-3}$ | $-12.703 \times 10^{-3}$ | 0.72      | $-10.983 \times 10^{-3}$ | 14.16     |
| $Y'_r$ | $1.811 \times 10^{-3}$   | $1.679 \times 10^{-3}$   | -7.29     | $1.149 \times 10^{-3}$   | -36.54    |
| $N'_r$ | $-1.597 \times 10^{-3}$  | $-1.493 \times 10^{-3}$  | 6.51      | $-2.064 \times 10^{-3}$  | -29.24    |

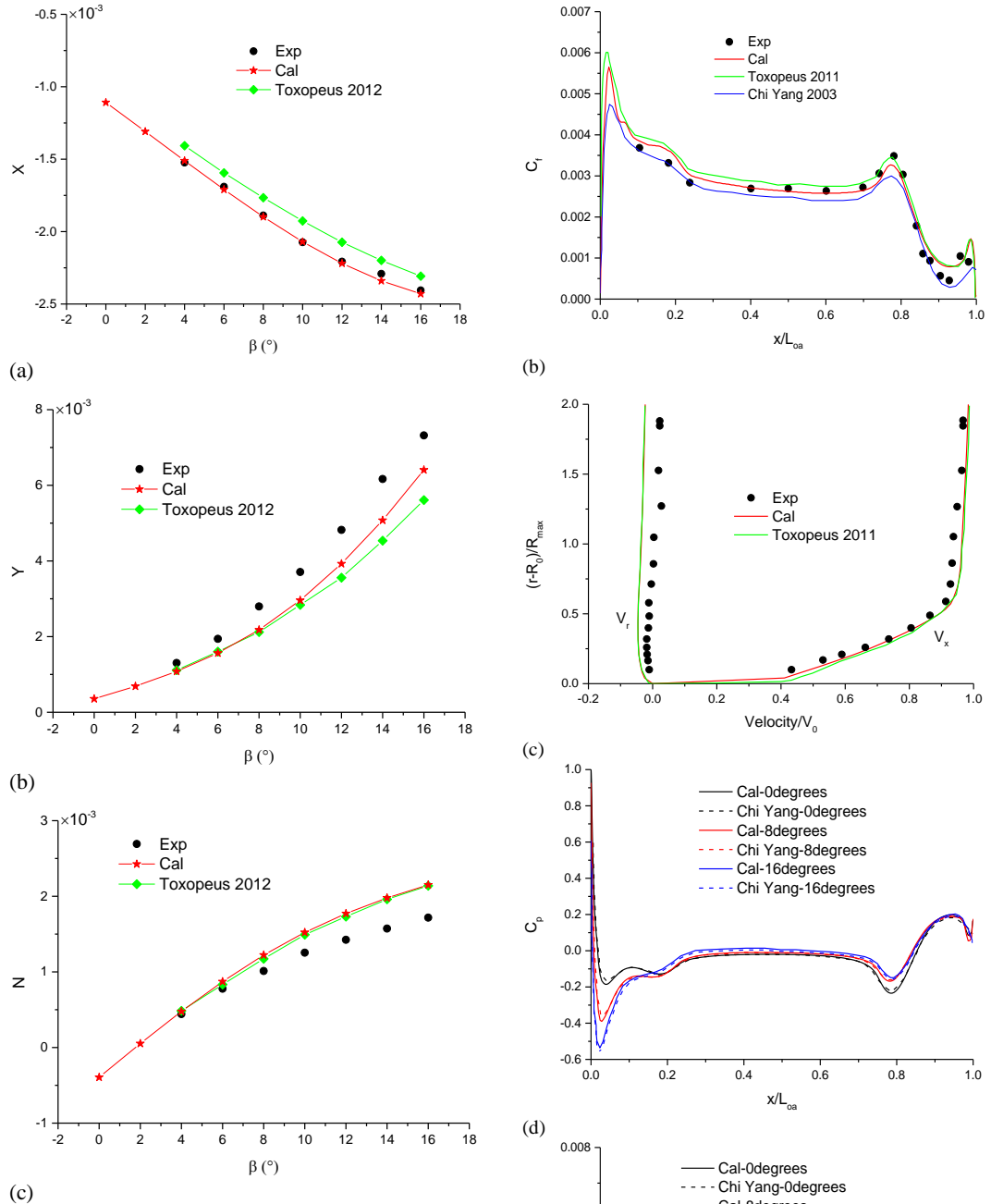


**Fig. 3. (a)-(c)** Non-dimensional drag, lateral force and yaw moment as a function of the drift angle in steady turn ( $\gamma = 0.37$ ).

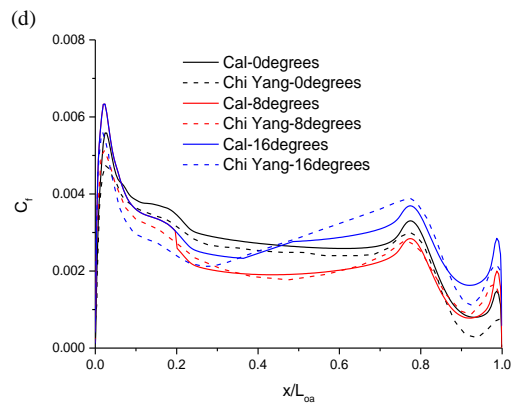
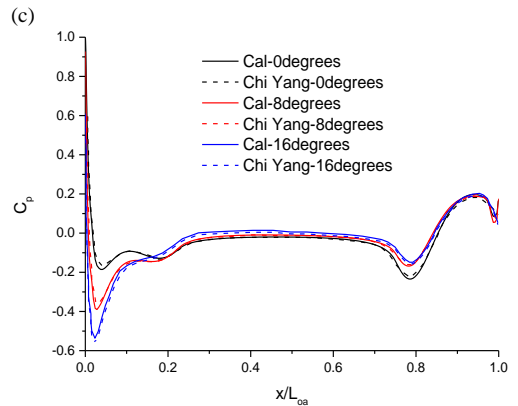
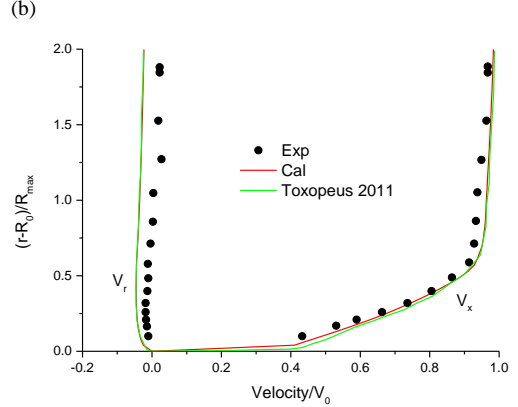
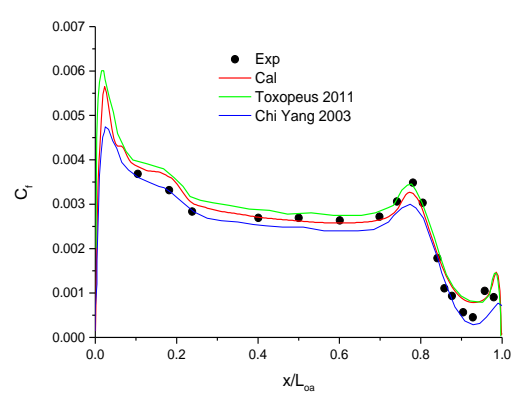
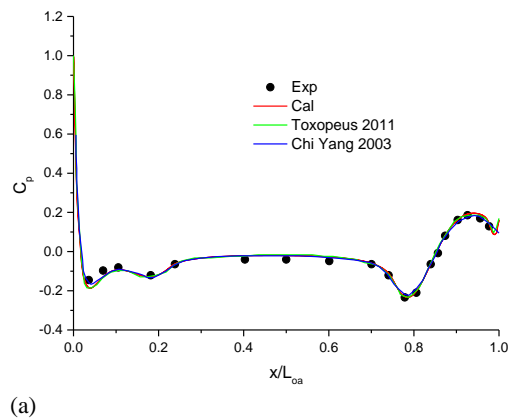


**Fig. 4. (a)** Pressure coefficients along the hull, **(b)** skin friction coefficients along the hull, **(c)** velocity profile at  $x/L_{oa} = 0.978$ , **(d)** comparison of computed and literature pressure coefficients along the hull, **(e)** comparison of computed and literature skin friction coefficients along the hull

Also shown are the percentage errors for estimates made using ASE methods. It can be concluded that the CFD method is more accurate than the ASE methods

#### 4.2 Pressure and Velocity Distribution

Fig. 4 (a) and (b) respectively present a comparison of the computed pressure and skin friction coefficients along the right meridian line of the hull with experimental data and literature values from Toxopeus (2011) and Yang (2003). The numerical predictions are in very good agreement with the experimental results. Fig.4 (c) shows results for the streamwise  $V_x$  and radial velocities  $V_r$  at  $x/L_{oa} = 0.978$  in the aft part of the hull. The difference between computed results and literature values is almost negligible. Comparing the computed results with the experiments, it is observed that the trends in the development of the boundary layer are very well predicted, but quantitative discrepancies are seen, especially at the very aft stern region. Fig.4 (d)-(e) show a comparison of computed pressure and skin friction coefficients along the right meridian line of the hull at zero, 8 and 16 degrees of angle of drift, respectively. Although some discrepancies are found, the trends correspond well.

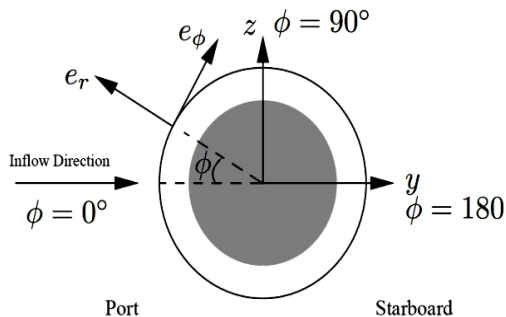


**Fig. 5. Definition of circumferential angle  $\phi$ .**

For the rotating arm test simulation, surface pressure coefficients at  $x/L_{oa} = 0.84$  are compared with experimental results, see Fig. 6. They are presented using the circumferential angle  $\phi$ , which is defined in Fig. 5. At the leeward side of the hull ( $120 < \phi < 240$ ), where flow separation occurs, the differences are noticeable. The agreement between the calculations and the experimental results is disappointing even though they show the similar trend. The reason is unknown and subject to further study.

#### 4.3 Vorticity and flow Field

Vorticity and velocity contours are used to study the nature of fluid motion in complex flow field. The flow pattern at different sections of the hull provides details of flow development over the hull length. The vorticity contours ( $\omega \times L_{pp}/V_0$ ) along the hull in 10 cut planes ( $x/L_{oa} = 0.2, 0.3, 0.4, 0.5, 0.6, 0.7, 0.8, 0.9, 1.0$  and  $1.1$ ) and axial velocity ( $V_x/V_0$ ) contours at  $x/L_{oa} = 0.978$  are shown in

Figs.7-9 for three angles of drift (0, 8 and 16 degrees) both in steady drift and in rotating arm, respectively. For both cases, it can be seen that there is a flow separation on the leeward side and as a consequence of this separation, two counter acting vortices are formed on the suction side. These vortices are transported further downstream and gain their strength all the way to the stern part. The flow separation happens earlier for  $16^\circ$  case when compared to that for lower angle of drift cases.

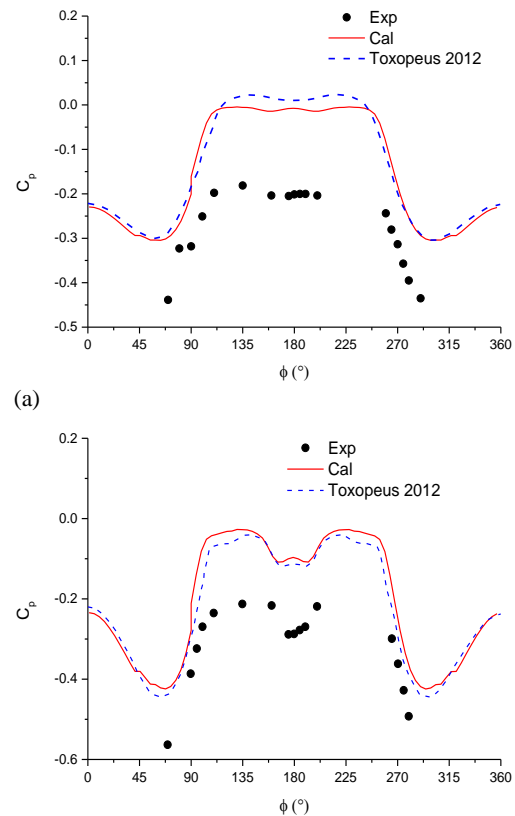
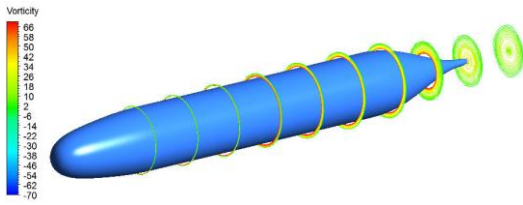


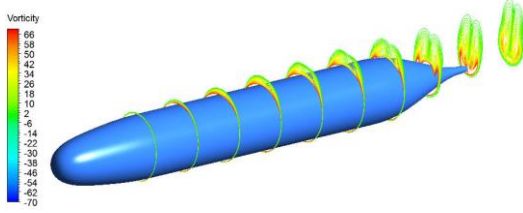
**Fig. 6. (a) Pressure distribution at  $x/L_{oa} = 0.84$ ,  $\gamma = 0.37$ ,  $\beta = 10^\circ$ . (b) pressure distribution at  $x/L_{oa} = 0.84$ ,  $\gamma = 0.37$ ,  $\beta = 16^\circ$**

In rotating flow the general levels of vorticity are much higher than that in the steady drift flow cases. This may, in part, be explained by the higher local incidence, but it seems likely that the flow curvature must also play a dominant role in the levels of vorticity experienced. The experiment conducted by Lloyd (1988) showed the same result.

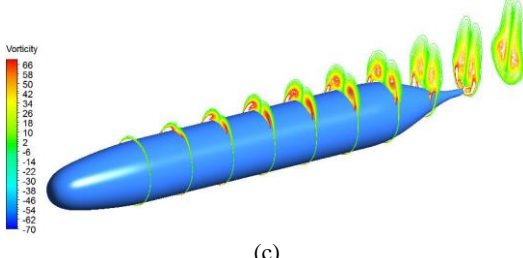
Fig. 9 and Fig.10 shows the axial velocity contours at  $x/L_{oa} = 0.978$  for two simulation cases, respectively. There is a large separated area at the leeward side of the hull. The vortices shed there are pulled down into the low pressure area at the leeward side of the hull and enter the propeller plane. At port side of the submarine the flow is smooth and follows the circular hull. At starboard Von Karman vortices typical of blunt-body flows are formed. These will also induce unsteady flow. The wake field of the submarine is therefore highly



(a)

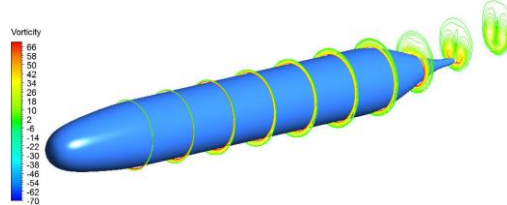


(b)

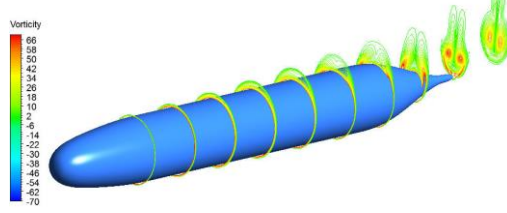


(c)

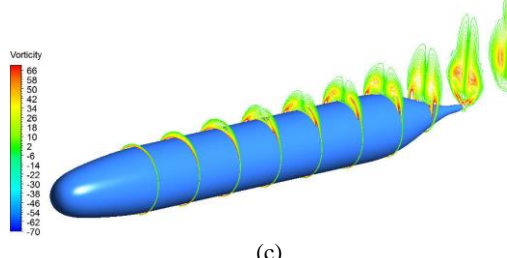
**Fig.7. Vorticity contours in 10 cut planes at 0, 8, 16 degrees angle of drift in steady drift tests( $\gamma = 0$ )**



(a)



(b)



(c)

**Fig. 8. Vorticity contours in 10 cut planes at 0, 8, 16 degrees angle of drift in rotating arm tests( $\gamma = 0.37$ )**

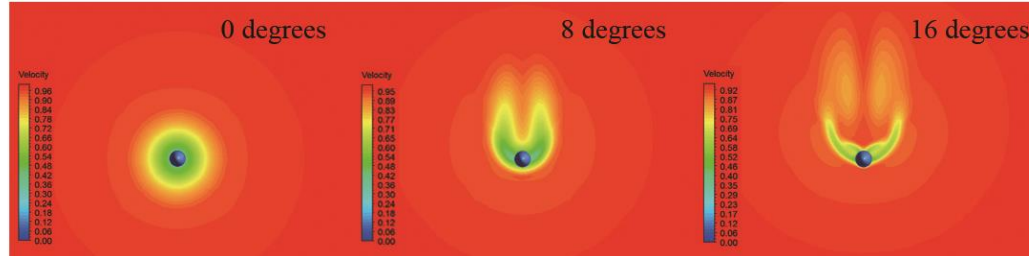


**Fig. 9. Comparison of computed wake field in steady drifts.**

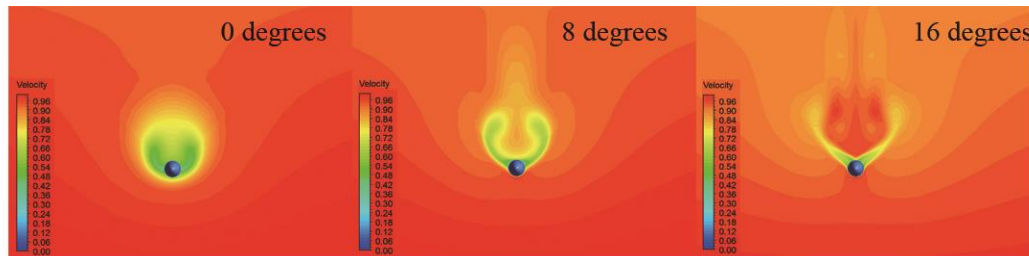


**Fig. 10. Comparison of computed wake field in rotating arm.**

asymmetrical and contains fierce vortical structures.

As the angle of drift increased, it can be observed that reverse flow areas are moved to the lateral side and getting larger. Noticeable differences can be observed for the wake field for steady drift and rotating motion.

## 5. CONCLUSION

Viscous-flow calculation around a generic submarine in maneuvering motion has been developed and verified. The method successfully resolved the flow around the hull, and the hydrodynamic forces and moment during steady drift and rotating motion. The pressure and skin

friction coefficients computed with present method are in good agreement with experimental measurements and literature values. The change of the flow structures due to different angles of drift are simulated successfully. It demonstrates that the same grid can be used to calculate both the steady drift cases and rotational cases which reduces the human labor in remeshing the domain every time. The comparison of flow field between steady drift and rotation improves our knowledge in these two kinds of flow motion, which differ a lot with each other. This paper has established a first step toward the goal of predicting the forces and moments for a fully appended submarine while maneuvering. Further efforts can be devoted to improving the accuracy of the predictions, where more advanced turbulence models (DDES or LES) may be used.

#### ACKNOWLEDGEMENTS

Part of the work presented here was funded by the National Natural Science Foundation of China (No. 51179199). Their support is greatly acknowledged.

#### REFERENCES

- Cao, L. S. and J. Zhu (2014). Prediction of submarine hydrodynamics using CFD-based calculations and RBF neural network. *Journal of Ship Mechanics* 18(3), 221-230.
- Carrica, P. and F. Ismail (2012). Turn and zigzag maneuvers of a surface combatant using a URANS approach with dynamic overset grids. *Journal of Marine Science and technology* 18(2), 166-181.
- De Barros, E. A., Dantas, J. L., Pascoal, A. M., *et al.* (2008). Investigation of normal force and moment coefficients for an AUV at nonlinear angle of attack and sideslip range. *IEEE Journal of Oceanic Engineering* 33(4), 538-549.
- De Barros, E. A., A. Pascoal and E. de Sa (2006). Progress towards a method for predicting AUV derivatives. *Proc. IFAC Manoeuvring Control Marine Crafts*.
- Feldman, J. P. (1995). Method of performing captive-model experiments to predict the stability and control characteristics of submarines. *David Taylor Research Center*.
- Groves, N. C., T. T. Huang and M. S. Chang (1989). Geometric characteristics of DARPA SUBOFF models :(DTTC Model Nos. 5470 and 5471). *David Taylor Research Center*.
- Hochbaum, A. C. (1998). Computation of the turbulent flow around a ship model in steady turn and in steady oblique motion. *Proceedings of 22th Symposium on Naval Hydrodynamics*, Washington, America.
- Holmes, E. P. (1995). Prediction of hydrodynamic coefficients utilizing geometric considerations. *Naval Postgraduate School*, Monterey, California.
- ITTC quality manual. (1999). Uncertainty analysis in CFD and guidelines for RANS codes. *Interim Recommended Procedure Prepared by Resistance Committee of 22nd ITTC*, Shanghai, China.
- Lloyd, A. R. (1988). Experiments to investigate the vorticity shed by a body of revolution in curved flow. *Technology Common to Aero and Marine Engineering* 73-84.
- Lloyd, A. R. and I. M. Campbell (1986). Experiments to investigate the vortices shed from a submarine-like body. In *Proc 59th AGARD Fluid Dynamics Panel Symp*, Aix-en-Provence, France 7-10.
- Nahon, M. (1993). Determination of undersea vehicle hydrodynamic derivatives using the USAF Datcom. In *OCEANS'93*, II283-II288.
- Peterson, R. S. (1980). Evaluation of semi-empirical methods for predicting linear static and rotary hydrodynamic coefficients. *NCSC TM-291-80*.
- Phillips, A. B., Turnock, S. R. and Furlong, M. (2010). Influence of turbulence closure models on the vortical flow field around a submarine body undergoing steady drift. *Journal of Marine Science and technology* 15(3), 201-217.
- Rajabi, E. and M. R. Kavianpour (2014). A modified time advancement algorithm for optimizing channel flow analysis in direct numerical simulation method. *Journal of Applied Fluid Mechanics* 7(2), 287-297.
- Roddy, R. F. (1990). Investigation of the stability and control characteristics of several configurations of the DARPA SUBOFF model (DTTC model 5470) from captive-model experiments. David Taylor Research Center.
- Sakthivel, R., S. Vengadesan and S. K. Bhattacharyya (2011). Application of non-linear  $k - \epsilon$  turbulence model in flow simulation over underwater axisymmetric hull at higher angle of attack. *Journal of Naval Architecture and Marine Engineering* 8(2), 149-163.
- Simonsen, C. D. and F. Stern (2003). Verification and validation of RANS maneuvering simulation of Esso Osaka: effects of drift and rudder angle on forces and moments. *Computers & fluids* 32(10), 1325-1356.
- Stern, F., Z. Y. Wang and J. M. Yang (2014). Recent progress in CFD for naval architecture and ocean engineering (keynote speaker), *Proc of the 11<sup>th</sup> International Conference on Hydrodynamics (ICHD 2014)*, Singapore.
- Stern, F., J. Yang and Z. Wang (2013). Computational ship hydrodynamics: nowadays and way forward. *International Shipbuilding Progress* 60(1), 3-105.
- Toxopeus, S. L. (2011). Practical application of viscous-flow calculations for the simulation of manoeuvring ships, PhD thesis. *Maritime*

- Research Institute Netherlands (MARIN).
- Toxopeus, S. L., P. Atsavapranee and W. Eric (2012). Collaborative CFD exercise for a submarine in a steady turn. *Proceedings of ASME 31st International Conference on Ocean, Offshore and Arctic Engineering*, Rio de Janeiro, Brazil.
- Vaz, G., S. L. Toxopeus and S. Holmes (2010). Calculation of manoeuvring forces on submarines using two viscous-flow solvers. *Proceedings of the ASME 2010 29th International Conference on Ocean, Offshore and Arctic Engineering*, Shanghai, China.
- Wang, Y., Y. Xin and Z. Gu (2014). Numerical and experimental investigations on the aerodynamic characteristic of three typical passenger vehicles. *Journal of Applied Fluid Mechanics* 7(4), 659-671.
- Yang, C. and R. Lohner (2003). Prediction of flows over an axisymmetric body with appendages. *The 8th International Conference on Numerical Ship Hydrodynamics*, Busan, Korea.
- Zhang, Z. R. (2010). Verification and validation for RANS simulation of KCS container ship without/with propeller. *Journal of Hydrodynamics, Ser. B* 22(5), 932-939.